Transient heat transfer of deforming droplets at high Reynolds numbers

Matthias Hase and Bernhard Weigand
Institute of Aerospace Thermodynamics, University of Stuttgart, Stuttgart, Germany

Received October 2002
Accepted January 2003

Keywords *Volume measurement, Surface texture, Heat transfer*

Abstract *A numerical study of heat transfer enhancement due to the deformation of droplets at high Reynolds numbers is described. The two phase-flow has been computed with a 3D DNS program using the volume-of-fluid method. The droplets are deformed because of the surrounding gas stream especially due to a sudden rise of flow velocity from zero to U_i. As the governing non-dimensional parameter the Weber number of the droplets has been varied between 1.3 and 10.8 by assuming different surface tensions at Reynolds numbers between 360 and 853. The dynamical behavior of the droplets as a function of the Weber and the Ohnsorge number are in good agreement with experimental results from the literature. At the highest Reynolds number Re = 853, a significant dependency of Nu on We has been found. The comparison of a Nusselt number computed with the real surface area with a Nusselt number computed with the spherical surface area shows that the heat transfer increases not only due to the droplet motion but also due to the larger surface area of the deformed droplet.*

Introduction

The process of heat transfer between a disperse and continuous phase is an important multiphase flow problem in evaporating systems with numerous practical applications, e.g. industrial sprays in gas turbines and automotive engines, among others. Because of the high velocities in these applications the disperse phase is deformed by the aerodynamic forces of the continuous phase. The mentioned flow regime in the present simulation occurs after the primary breakup in a spray. Then the droplets from the dense core region were moved to the outer region of the spray. The velocity of the outer region is much smaller than the velocity in the core region which is driven by the injection pressure. Therefore, the droplets are strongly decelerated and due to this the deformation and breakup of the liquid droplets occur.

The process can be studied experimentally by shock tube experiments (Hsiang and Faeth, 1992, 1995). In the study of Hsiang and Faeth, only the deformation and breakup without heat transfer has been the topic of interest.

The authors would like to thank the "Deutsche Forschungsgemeinschaft" (DFG) for the financial support of this project and the High-Performance-Computing-Center Stuttgart (HLRS) for the computational time on the Cray T3E.

International Journal of Numerical Methods for Heat & Fluid Flow
Vol. 14 No. 1, 2004
pp. 85-97

0961-5539
DOI 10.1108/09615530410511649

Non-dimensional parameters characterizing this mechanism are the Weber number We, specifying the intensity of kinetic forces relative to the stabilizing surface tension forces, and the Ohnsorge number Oh, quantifying the effect of internal viscous forces relative to the surface tension forces

$$\mathrm{We} = \frac{U^2 D_0 \rho_\mathrm{G}}{\sigma}, \qquad \mathrm{Oh} = \frac{\mu_\mathrm{L}}{\sqrt{\rho_\mathrm{L} D_0 \sigma}}.$$

where the subscripts L and G indicate the liquid gaseous phases, respectively. Furthermore U, ρ, μ, σ and D_0 are the relative velocity between droplet and gas stream, the density, the dynamic viscosity, the surface tension and the spherical diameter of the droplet, respectively. In dependency of Weber and Ohnsorge number, Hsiang and Faeth specify the transition between different deformation and breakup regimes. These results have been used as a validation of the droplet deformation. The breakup regimes are not the topic of this present study. The breakup gives only an upper limit for the Weber number. The critical Weber number for sudden shock loading is given by $\mathrm{We}_{\mathrm{crit}} \approx 13$ under the restriction of negligible viscosity effects $\mathrm{Oh} < 0.2$ (Hsiang and Faeth, 1995).

Up to now the heat transfer from deformed disperse particles in high Reynolds number flow ($\mathrm{Re} > 270$) has been studied rarely, because of the fully 3D, transient flow regime which has been considered. Most authors who dealt with this topic paid attention to only one of the two problems of high Reynolds number or fully 3D flow and deformation.

Nguyen *et al.* (1993) computed the transient heat transfer of a spherical, liquid droplet with a hybrid spectral scheme. The study of Feng and Michaelides (2000, 2001) dealt only with heat transfer at high Reynolds numbers but without deformation of the liquid phase. The convective heat transfer of non-spherical solid particle has been investigated numerically by Comer and Kleinstreuer (1995). Their study is limited to Reynolds numbers between 40 and 120. Haywood *et al.* (1994) computed the transient heat transfer and evaporation of deformed droplets at intermediate Reynolds numbers ($10 < \mathrm{Re} < 100$) with transient, axisymmetic deformation using a finite volume based numerical technique. Other publications from the same research group and with same numerical approach (Haywood *et al.*, 1989; Renksizbulut and Haywood, 1998) dealt with spherical, evaporating droplets.

Experimental studies on heat transfer from liquid droplets especially for deformed droplets are very rare. Up to now, the correlation of Ranz and Marshall (1952) is used for the computation of heat transfer coefficients of spherical or deformed droplets.

In the present study, the influence of transient deformation on the heat transfer has been investigated numerically at high Reynolds numbers with a fully 3D approach and no restriction on the deformation of the disperse phase.

The efficiency of the program for the computation of the dynamics of strongly deformed droplets has been presented by Rieber and Frohn (1999). The validation of the energy equation is reported in Hase and Weigand (2001).

Analysis and numerical method

The inhouse 3D CFD program, free surface 3D (FS3D), has been developed to compute the Navier-Stokes equations for incompressible flow with free surfaces. The equations are solved without using a turbulence model with direct numerical simulation (DNS). The governing equations for momentum and mass transport are

$$\frac{\partial(\rho\mathbf{u})}{\partial t} + \nabla\cdot[(\rho\mathbf{u})\otimes\mathbf{u}] = -\nabla p + \nabla\cdot\mu[\nabla\mathbf{u} + (\nabla\mathbf{u})^{\mathrm{T}}] + \nabla\cdot\mathbf{T}_{\mathrm{cs}} \tag{1}$$

$$\nabla\cdot\mathbf{u} = 0, \tag{2}$$

where $\mathbf{T}_{\mathrm{cs}}$ is the capillary stress tensor which adds the surface tensor force to the momentum equation. Furthermore, $\mathbf{u}$ and p are the velocity vector and pressure, respectively.

Additionally, the energy equation is solved. For the above mentioned incompressible flow and for a fluid with constant fluid properties in each phase, the energy equation is decoupled from the equations of motion. Therefore, the energy equation can be solved after the computation of the flow field. The energy equation has been implemented in the temperature form

$$\frac{\partial}{\partial t}(\rho c_{\mathrm{p}} T) + \nabla\cdot(\rho c_{\mathrm{p}}\mathbf{u}T) = \nabla\cdot(k\nabla T) + \Phi. \tag{3}$$

where T is the thermodynamic temperature, c_{p} the specific heat at constant pressure and k the heat conductivity. The dissipation term Φ can be neglected for all mentioned flows due to the low Eckert number.

In two phase flows, additional information about the interface position between the disperse and the continuous phase is required. There are two different approaches to manage this task. The first one is the explicit tracking of the interface (front-tracking) and the other the tracking of the disperse phase (volume-tracking). In FS3D, a volume-tracking method, well known as the volume-of-fluid (VOF) method, is used (Hirt and Nichols, 1981). In the VOF-method, an additional transport equation

$$\frac{\partial f}{\partial t} + \nabla\cdot(\mathbf{u}f) = 0 \tag{4}$$

for the volume fraction of the disperse phase is solved. The variable f is called the VOF-variable. The VOF-variable is

$$f = \begin{cases} 0 & \text{in the continuous phase} \\ 0 < f < 1 & \text{at the interface} \\ 1 & \text{in the disperse phase} \end{cases} \quad (5)$$

With the VOF-variable the change of the fluid properties across the interface can be computed by using the equations

$$\rho(\mathbf{x}, t) = \rho_{\mathrm{d}} + (\rho_{\mathrm{c}} - \rho_{\mathrm{d}}) f(\mathbf{x}, t) \quad (6)$$

$$\mu(\mathbf{x}, t) = \mu_{\mathrm{d}} + (\mu_{\mathrm{c}} - \mu_{\mathrm{d}}) f(\mathbf{x}, t) \quad (7)$$

where the subscripts c and d indicate the continuous disperse phases, respectively. Additional fluid properties like the specific heat c_{p} and the heat conductivity k are obtained in the same way with the VOF-variable. To ensure a sharp interface and to suppress numerical dissipation of the disperse phase in each time step, the interface is reconstructed by using the piecewise linear interface reconstruction computation (PLIC) method (Rider and Kothe, 1998). After the reconstruction, the disperse phase is transported on the basis of the reconstructed distribution of the disperse phase.

The spatial discretization is realized by a structured finite volume scheme on a staggered grid. In each phase, the discretization is second-order accurate. Because of the high gradients over the interface, a limiter is used to prevent the generation of oscillations and spurious solutions. The program is parallelized with domain decomposition using the communication library MPI. A multigrid solver is included to solve the Poisson equation for the pressure. The features of the program with the description of the solution algorithm has been reported by Rieber (1999). Additionally a coordinate transformation from the inertial system to the droplet system is implemented (Rieber *et al.*, 2000) to track the droplet for a longer time without generating very large computational domains.

Simulation results

Computational domain and fluid properties

In the present simulations, the liquid has been assumed to have the properties of water at 20°C except for the dynamic viscosity and the surface tension. The dynamic viscosity is $\mu_{\mathrm{L}} = 10 \times \mu_{\mathrm{H_2O}} = 1 \times 10^{-3}\,\mathrm{kg/(ms)}$ and the surface tension can be taken from Table I. The higher viscosity has been chosen to avoid *parasitic currents* (Scardovelli and Zaleski, 1999). As mentioned earlier, for the surrounding gas the properties of air has been assumed. The initial temperature of the liquid was $T_{\mathrm{L}} = 350\,\mathrm{K}$ and $T_{\mathrm{G}} = 293.15\,\mathrm{K}$ for the gaseous phase.

The computational domain is displayed in Figure 1. The 3D channel geometry for a droplet with the diameter $D = 2 \times 10^{-3}\,\mathrm{m}$ is $x = 24 \times 10^{-3}\,\mathrm{m}$, $y = 12 \times 10^{-3}\,\mathrm{m}$ and $z = 12 \times 10^{-3}\,\mathrm{m}$. For other droplet diameters, the channel size has been chosen in a similar way to obtain the same geometric ratios

D_0 (mm)	U_0 (m/s)	$\sigma \times 10^{-3}$ (N/m)	$\mathrm{Re} = U_0 D_0 \rho_G / \mu_G$	$\mathrm{We} = U_0^2 D_0 \rho_G / \sigma$	$\mathrm{Oh} = \mu_L / \sqrt{\rho_L D_0 \sigma}$
1.2	4.5	22.0	360	1.33	6.15×10^{-2}
1.2	4.5	12.0	360	2.43	8.33×10^{-2}
1.2	4.5	6.0	360	4.86	0.117
1.2	4.5	3.5	360	8.33	0.154
1.2	4.5	3.0	360	9.72	0.166
1.2	4.5	2.8	360	10.41	0.172
1.5	5.2	36.0	520	1.35	4.30×10^{-2}
1.5	5.2	20.0	520	2.43	5.77×10^{-2}
1.5	5.2	10.0	520	4.86	8.18×10^{-2}
1.5	5.2	5.9	520	8.25	0.106
1.5	5.2	5.0	520	9.73	0.115
1.5	5.2	4.5	520	10.82	0.122
2.0	6.4	73.0	853	1.35	2.62×10^{-2}
2.0	6.4	40.0	853	2.46	3.52×10^{-2}
2.0	6.4	20.0	853	4.92	5.00×10^{-2}
2.0	6.4	12.0	853	8.19	6.45×10^{-2}
2.0	6.4	10.0	853	9.83	7.07×10^{-2}
2.0	6.4	9.0	853	10.92	7.45×10^{-2}

Table I.
Summary of simulation conditions

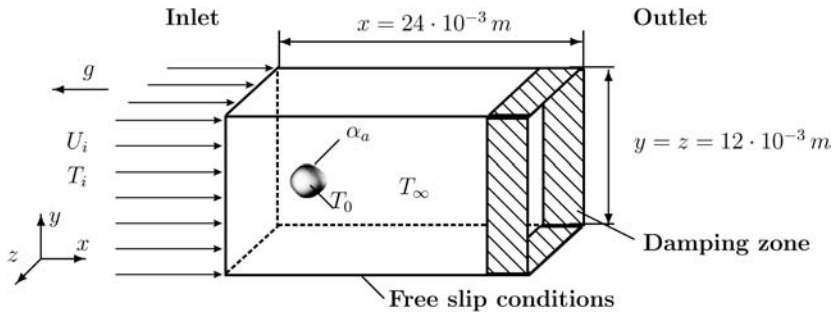

Figure 1.
Channel geometry and boundary conditions for the computation of droplet diameter $D = 2 \times 10^{-3}$ m

between droplet diameter and channel length. The gravitational force acts in the negative x-direction. The inlet boundary is on the left with a constant inflow velocity and temperature U_i, $T_i = T_G = T_\infty$. On the right, an outlet boundary with an additional damping zone is placed. The damping zone avoids backflow into the computational domain. At the other boundaries, Dirichlet boundary conditions for the y- and z-velocities $v = w = 0$ and Neumann boundary conditions for the x-velocity $(\mathrm{d}u/\mathrm{d}x)_W = 0$ are used.

The initial droplet shape is spherical without a deformation due to the surrounding gas stream. Hence, the droplet receives something like a strike from the first approaching flow. This condition is similar to the condition in the shock tube of Hsiang and Faeth (1995) and it leads also to an initial deformation

and oscillation of the droplet. The amplitude of the deformation and the number of oscillation periods depend on the Weber and the Ohnsorge numbers.

Deformation of the droplet

First, the dynamic behavior of the droplets is studied. The deformation rate shown as a ratio of A/A_0, where A is the surface area of the deformed droplet and A_0 the surface area of a spherical droplet with the same volume, is displayed in Figure 2 for the Reynolds number Re = 853. The deformation is plotted in dependency of the Fourier number $\mathrm{Fo} = ta_G/R_0^2$ which is a non-dimensional time. A summary of the simulation conditions and the non-dimensional parameters Re and Oh is given in Table I.

Because of the higher kinetic energy proportional to the surface tension forces of the flow described by the higher Weber number, the droplets with higher Weber numbers are deformed much more from the first approaching flow. For a Weber number We = 10.9, the ratio of the surface areas is $A/A_0 = 1.175$ for the first oscillation in prolate shape. For We = 4.9, the deformation is still $A/A_0 = 1.04$ and only $A/A_0 = 1.01$ for We = 1.35. After this strong, first deformation (for the higher Weber numbers) in the oblate direction, the droplet oscillates to a nearly spherical shape and back to an oblate shape. Without a second time oscillating through the spherical state, the droplet stays in the oblate deformation state with only small changes. These changes occur due to the highly transient flow around the droplet. At this time the surface tension force is not able to form a spherical droplet against the aerodynamic forces from the surrounding flow. This behavior – the strongest deformation due to the initial approaching flow, an oscillation to the spherical state and then back to the oblate deformation – can only be seen for the Weber numbers We = 9.8 and 10.9.

To point out the deformation regime of a droplet with a higher Weber number the droplet shape for We = 9.8 is shown in Figure 3(a) with the surrounding velocity field and in Figure 3(b) with the temperature and the velocity field. In Figure 3(a) and (b), a cut from the 3D geometry through

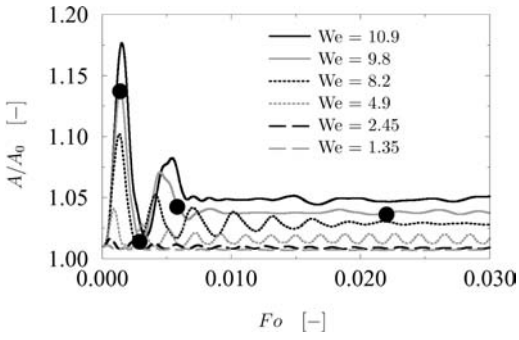

Figure 2.
Non-dimensional ratio A/A_0 in dependency of the time Fo. The black marks are the times in Figure 3

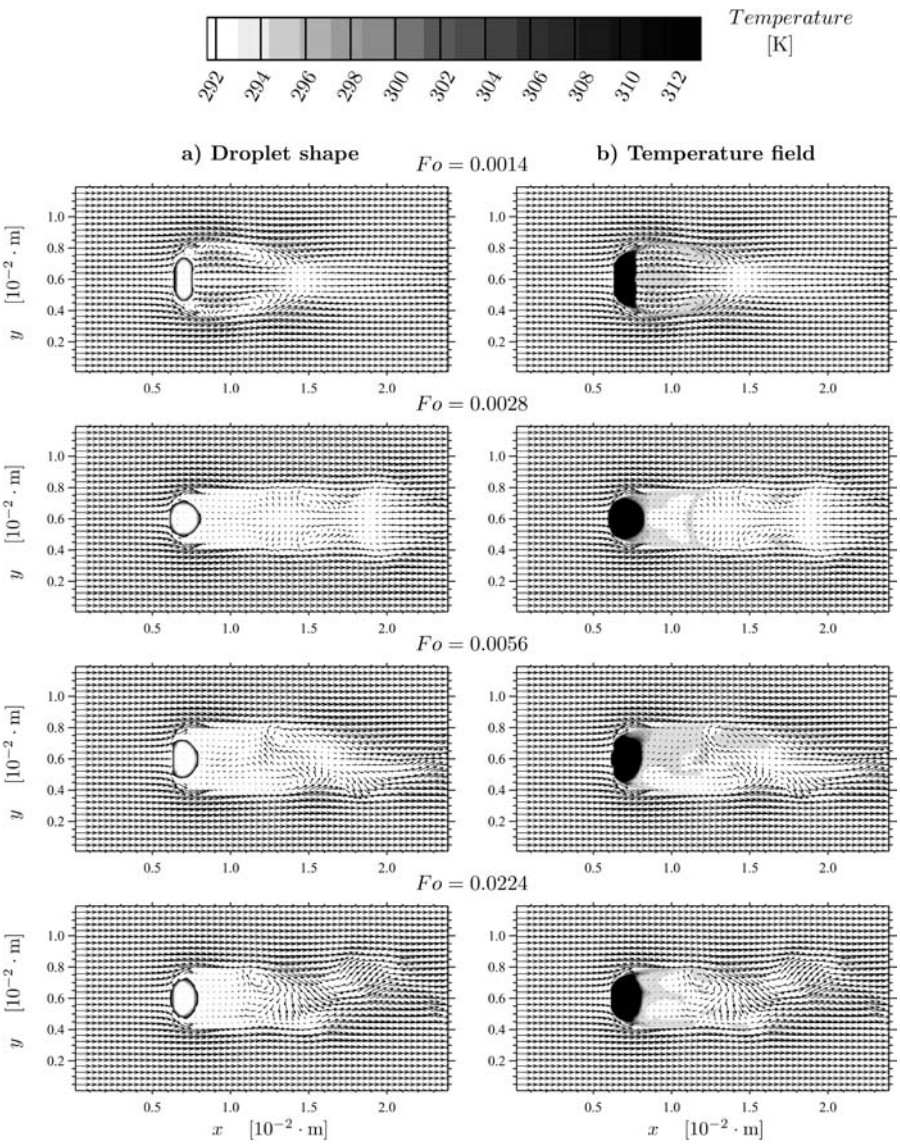

Figure 3.
Velocity and temperature fields around a deformed droplet with the diameter $D = 2\,\text{mm}$ in dependency of Fo

the center of the droplet in the *xy*-plane is displayed. The influence of the deformation regime on the temperature field will be discussed later. The respective times of Figure 3(a) and (b) are marked by the black circles in Figure 2 for We = 9.8.

For the first displayed droplet shape at Fo = 0.0014, the maximum deformation in oblate direction is reached. The ratio of the deformed to the spherical surface area is $A/A_0 \approx 1.14$ (Figure 2). The displayed flow field

around the droplet is at this time nearly symmetrical, which is mainly an effect from the initial conditions of the velocity. However, it has although taken into account that the droplet motion influences the nearby flow field very much. This can be seen from the high velocities in the recirculation zone behind the droplet which are pointing to the rear side of the droplet. At Fo = 0.0028, the droplet reaches a nearly spherical shape again. Only in the front the droplet is flattened. After the displayed state, the droplet oscillates back to an oblate deformation period. In Figure 3, at Fo = 0.0056, the transition region between the oblate and final shapes is displayed. It can also be seen that the flow field at this time is fully 3D. The final shape is shown for Fo = 0.0224. In both figures, the flattening in front of the droplet can be observed. This flattening occurs in agreement with Hsiang and Faeth (1995) who found "dome-shaped" drops for this range of Weber and Ohnsorge numbers.

For lower Weber numbers We = 1.3, 2.45, 4.9 and 8.2, the droplet oscillation is different from the behavior described before. For the Weber numbers We = 9.8 and 10.9, the oscillation continues only for two periods without reaching a prolate droplet shape. For the other Weber numbers from 1.35 to 8.2 the oscillations continue and only for We = 8.2 a nearly steady deformation reaches at Fo $\approx$ 0.025 for the displayed time interval. Additionally, the droplets oscillate between an oblate and a prolate deformation. The reason for this is the higher surface tension force for these cases which introduces a larger kinetic energy into the liquid phase. This energy is able to deform the droplet from the spherical state to the prolate or oblate deformation state, respectively. The oscillation for We = 4.9 continues over the whole time without a significant damping. For We = 2.45 and 1.35, the oscillation is not damped completely during the displayed time interval but the amplitudes are very small and hardly visible.

In Figure 3(b), the temperature and the velocity field of the deformed droplet and the surrounding gas are displayed. To make the temperature difference in the gas stream visible the temperature scale is chosen between 293 and 312 K in spite of a droplet temperature of 350 K. Hence the droplet and the nearby region are shown in black for $T > 312$ K. At Fo = 0.0014, a temperature decrease in the gas stream can be seen at the edge of the disc and behind the disc in the center of the recirculation zone. For Fo = 0.0056 and 0.0224, the fully 3D character of the flow and temperature fields are visible.

Heat transfer computation

After the investigation of the droplet deformation due to the surrounding gas stream the influence of the deformation on the heat transfer has been studied. To perform this study a time and space averaged Nusselt number

$$\mathrm{Nu_m} = \frac{D_0 \alpha_\mathrm{a}}{k_\mathrm{G}} \tag{8}$$

has been computed from the temperature evolution in the simulations. The heat transfer coefficient α_a has been obtained from the energy balance

$$-\rho_L V c_{v,L} \frac{\partial T_m}{\partial t} = -A_0 \alpha_a (T_{W,m} - T_\infty), \tag{9}$$

where c_v is the specific heat at constant volume, T_m the averaged droplet temperature, $T_{W,m}$ a time and space averaged wall temperature and T_∞ denotes the temperature in the undisturbed gas flow. The subscript 0 indicates the initial (spherical) state of the surface area A and diameter D. Explained in discrete values the heat transfer coefficient α_a has been computed according to

$$\alpha_a = \frac{\rho_L V c_{v,L}}{A_0 (T_{W,m} - T_\infty)} \frac{\Delta T_m}{\Delta t}. \tag{10}$$

It has to be noted that because of the short time scales in this study the displayed Nu_m is far away from the thermal fully developed state Nu_∞. For example, the Nusselt number from the correlation given by Ranz and Marshall (1952) for $Re = 853$ and $Pr = 0.714$ is $Nu_\infty = 17.5$. The present study deals not with the simulation of this Nu_∞ for long time periods but only with the strongly transient period for droplet dynamic and heat transfer at the beginning of this process. Therefore, in Figure 4, at $Fo = 0.03$ there is no level asymptote in the Nusselt number evolution. The Nusselt number decreases further on, but with a much smaller gradient. In many applications this first time period is of great importance due to the short time scale and the strong transient behavior of the whole process.

In Figure 4, the evolution of Nu_m in dependency of Fo for three different Reynolds numbers $Re = 360$, 520 and 853 is depicted. The Weber number has been varied between $1.3 \leq We \leq 10.8$ in the simulations. It has been found that for all Reynolds numbers, the heat transfer depends on the Weber number. For the shown time interval, Nu_m increases with increasing Weber numbers. The dependency becomes stronger for higher Weber numbers and higher Reynolds numbers in most cases. Because of the improvements in the computer program, the Nusselt numbers in Figure 4 for the higher Weber numbers and larger times (Fo) are different from the one shown by Hase and Weigand (2002). One of the present improvements eliminated a programming error which resulted in slight deviations in the computation of the Nusselt number for highly dynamical processes. For the highest Reynolds number $Re = 853$, the dependency is more pronounced. The Nusselt numbers differ from $Nu_m \approx 22.5$ ($We = 1.35$) to $Nu_m \approx 27$ ($We = 10.9$) which is a difference of about 20 percent. At $Fo \approx 0.005$, the influence of the deformation can be seen with a maximum in Nu_m for $We = 4.9$, 8.2, 9.8, and 10.9. In comparison with the non-dimensional surface area from Figure 2 at approximately this time the second maximum occurs also in the surface area evolution. The maximum in

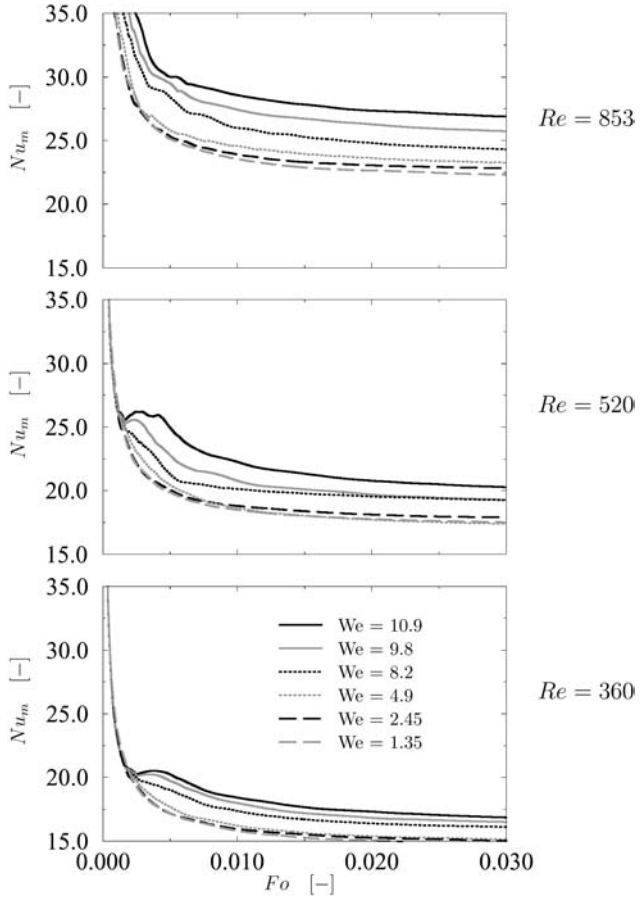

Figure 4.
Time and space averaged Nusselt number Nu_m in dependency of Fo for different Reynolds and Weber numbers

the Nusselt number evolution occurs because the first maximum in the deformation has cut due to the chosen Nusselt number interval. (It will be shown in Figure 5 for We = 10.8 and Re = 853 that this peak occurs.) The peaks from Nu_m in Figure 4 appear at earlier times for lower Weber numbers which is also in agreement with the behavior of the deformation shown in Figure 2 for the surface area. For Re = 520, the dependency of Nu_m(We) is also clear for most Weber numbers. Only for We = 9.8 and 8.2, the curves of Nu_m reach the same value. A reason for this can be the eigenfrequency of the droplet which is very close to the stimulation frequency from the flow. The difference in the Nusselt numbers is about 14.3 percent (Nu_m(We = 1.3) ≈ 17.5, Nu_m(We = 10.9) ≈ 20). The influence of the deformation can be seen in the Nusselt number evolution for We = 8.2, 9.8 and 10.9 as well. For Re = 360, the dependency Nu_m(We) is not so pronounced but all Nusselt numbers show the expected evolution. The difference in the Nusselt numbers is 13.3 percent

($Nu_m(We = 1.3) \approx 15$, $Nu_m(We = 10.9) \approx 17$). It should be pointed out that the thermal boundary layer around the droplet is not resolved fine enough in the present computations ($128 \times 64 \times 64$). This could give rise to changes in the Nusselt number. However, a study will be carried out in the future to investigate the difference in the Nusselt number for much finer grids. Here it is presently unclear, if a fully grid independent calculation with high enough resolution of the thermal boundary layer can be received at the supercomputers in Stuttgart. First test indicates a systematic deviation of about ≤ 20 percent. The present results are qualitatively correct.

Another interesting phenomenon is the peak in the shape of the Nusselt number evolution for high Weber numbers which can be seen in Figure 4 for $Re = 520$ and $We = 10.8$ at $Fo = 0.003$ and which appears also at $Re = 853$ at the same Weber number (Figure 5). Here it has been considered that in equation (8), the surface area of the spherical droplet A_0 is used. The important question in this context is if this maximum occurs only due to the increased surface area of the deformed droplet A or if the heat transfer is enhanced also from the droplet motion and the flow regime. To investigate this problem in more detail, the heat transfer coefficient in equation (8) has been computed according to

$$\alpha_a = \frac{\rho_L V c_{v,L}}{A(T_{W,m} - T_\infty)} \frac{\Delta T_m}{\Delta t}, \tag{11}$$

where A is the real surface area of the deformed droplet. With this heat transfer coefficient, the Nusselt number is computed, which is shown in Figure 5 in comparison with the Nusselt number computed by equation (8) with A_0 for different Reynolds numbers and $We = 10.8$. As expected, the Nusselt numbers computed with the real surface area A are smaller than the Nusselt numbers computed with A_0 for both Reynolds numbers. But the most important result from Figure 5 is that the maximum in the Nusselt number evolution occurs also for the Nusselt number computed with the real surface area. This points out that the Nusselt number in this case is enhanced also due to the droplet oscillation and the flow regime which results from this oscillation.

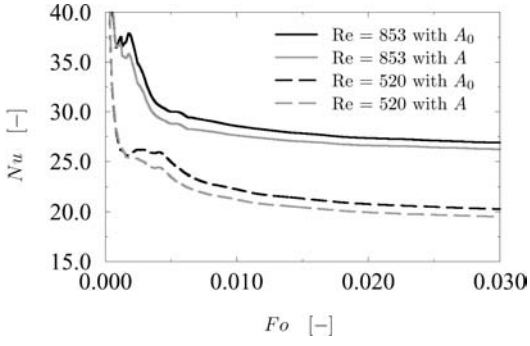

Figure 5.
Evolution of the Nusselt number computed with the real surface of the deformed droplet A and the surface of a spherical droplet A_0 in dependency of Fo for two Reynolds numbers

Finally, the dependency of the Nusselt number on the Reynolds number has been investigated. For the present study, it has been assumed that $Nu \sim Re^{\beta}$. The exponent β has been calculated from the Nusselt numbers shown in Figure 4. The results are displayed in Figure 6 as a function of Fo for different Weber numbers. All values of β are in the expected range of $Nu \sim Re^{1/2}$ which is the well known dependency for steady-state flows from the literature (Ranz and Marshall, 1952). For $We = 9.8$ and the comparison of the Nusselt number evolution for $Re = 853$ and 360 the largest values of β have been found for $Fo \geq 0.005$. In comparison with the value $We = 1.3$ for the same Reynolds numbers this is the expected behavior from Figure 4. The values of β for the change in the Nusselt number between $Re = 360$ and 520 are significantly smaller. It is interesting that β differs not very much for $We = 1.3$ but for $We = 9.8$ between the two Reynolds number intervals. Furthermore it is interesting to note that the exponent β is nearly constant for a given Weber number for $Fo \geq 0.01$. The reason for this deviation at early times are the maxima in the Nusselt number evolutions which do not occur later. Because of the different oscillation time of the droplets which appear because of the change in the surface tension these maxima occur at various times for the different Reynolds and Weber numbers.

Concluding remarks

An inhouse 3D CFD program (FS3D) has been modified and used to compute the heat transfer for deformed droplets at high Reynolds numbers. The deformation regimes of the droplets are in good agreement with experimental data from literature. The results for the heat transfer show the dependency of the Nusselt number on the Weber number. The dependency becomes stronger for higher Reynolds numbers. Furthermore, it is shown that the Nusselt number for deformed droplets is enhanced not only due to the droplet oscillation and the flow regime, which results from this oscillation, but also due to the larger surface area of the deformed droplets. The present study will be extended to a longer time scale in future work. A wider range of Reynolds number will be investigated as well.

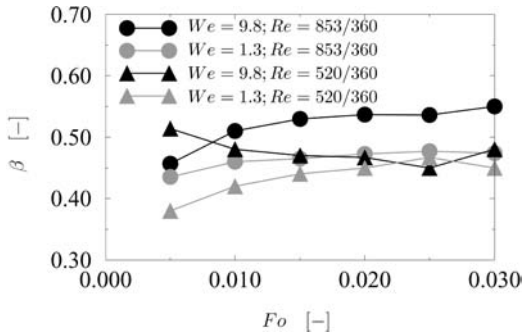

Figure 6.
Exponent β for $Nu \sim Re^{\beta}$ as a function of Fo for different Weber numbers. The Reynolds numbers denote which Nusselt numbers evolutions are compared

References

Comer, J.K. and Kleinstreuer, C. (1995), "Computational analysis of convection heat transfer to non-spherical particles", *Int. J. Heat Mass Transfer*, Vol. 38 No. 17, pp. 3171-80.

Feng, Z-G. and Michaelides, E.E. (2000), "A numerical study on the transient heat transfer from a sphere at high Reynolds and Peclet numbers", *Int. J. Heat and Mass Transfer*, Vol. 43, pp. 219-29.

Feng, Z-G. and Michaelides, E.E. (2001), "Heat and mass transfer coefficents of viscous spheres", *Int. J. Heat Mass Transfer*, Vol. 44 No. 23, pp. 4445-54.

Hase, M. and Weigand, B. (2001), "Numerical study of the temperature field of unsteady moving droplets and of the surrounding gas", *Proceedings ILASS-Europe 2001*, Zuerich.

Hase, M. and Weigand, B. (2002), "Direct numerical simulation of flow and heat transfer of a droplet with transient deformation due to the surrounding gas stream", *Proceedings WCCM V.*, Wien, Available at: http://wccm.tuwien.ac.at/

Haywood, R.J., Nafziger, R. and Renksizbulut, M. (1989), "A detailed examination of gas and liquid phase transient processes in convection droplet evaporation", *Journal of Heat Transfer*, Vol. 111, pp. 495-502.

Haywood, R.J., Renksizbulut, M. and Raithby, G.D. (1994), "Numerical solution of deforming evaporating droplets at intermediate Reynolds numbers", *Int. J. Heat Mass Transfer*, Vol. 37 No. 4, pp. 1401-9.

Hirt, C.W. and Nichols, B.D. (1981), "Volume of fluid (VOF) method for the dynamics of free boundaries", *Journal of Computational Physics*, Vol. 39, pp. 201-25.

Hsiang, L-P. and Faeth, G.M. (1992), "Near-limit drop deformation and secondary breakup", *Int. J. Multiphase Flow*, Vol. 18 No. 5, pp. 635-52.

Hsiang, L-P. and Faeth, G.M. (1995), "Drop deformation and breakup due to shock wave and steady disturbance", *Int. J. Multiphase Flow*, Vol. 21 No. 4, pp. 545-60.

Nguyen, H.D., Paik, S. and Chung, J.N. (1993), "Unsteady conjugate heat transfer associated with a translating spherical droplet: a direct numerical simulation", *Numerical Heat Transfer, Part A*, Vol. 24, pp. 161-80.

Ranz, W.E. and Marshall, W.R. (1952), "Evaporation from drops, Part II", *Chemical Engineering Progress*, Vol. 48 No. 4, pp. 173-80.

Renksizbulut, M. and Haywood, R.J. (1988), "Transient droplet evaporation with variable properties and internal circulation at intermediate Reynolds numbers", *Int. J. Multiphase Flow*, Vol. 14 No. 2, pp. 189-202.

Rider, W.J. and Kothe, D.B. (1998), "Reconstructing volume tracking", *Journal of Computational Physics*, Vol. 141, pp. 112-52.

Rieber, M. (1999), Numerische Modellierung der Dynamik freier Oberflächen in Zweiphasenströmungen, Technical Report Fr-235/43-1, DFG.

Rieber, M. and Frohn, A. (1999), "A numerical study on the mechanism of splashing", *International Journal of Heat and Fluid Flow*, Vol. 20 No. 5, pp. 455-61.

Rieber, M., Graf, F., Hase, M., Roth, N. and Weigand, B. (2000), "Numerical simulation of moving spherical and strongly deformed droplets", *Proceedings ILASS-Europe 2000*.

Scardovelli, R. and Zaleski, S. (1999), "Direct numerical simulation of free-surface and interfacial flow", *Annual Review Fluid Mechanics*, Vol. 31, pp. 567-603.